Journal of Materials Science: Materials in Electronics (2020) 31:11150–11158
https://doi.org/10.1007/s10854-020-03664-5

Fullerene (C_{60})-modulated surface evolution in $CH_3NH_3PbI_3$ and its role in controlling the performance of inverted perovskite solar cells

M. S. Patel[1] · Dhirendra K. Chaudhary[1,3] · Pankaj Kumar[2] · Lokendra Kumar[1]

Received: 27 January 2020 / Accepted: 22 May 2020 / Published online: 28 May 2020

Abstract

We report here the effect of fullerene (C_{60}) incorporation on the growth of $CH_3NH_3PbI_3$ perovskite crystals and the effect on photovoltaic performance of perovskite solar cells (PSCs) prepared in inverse geometry. Incorporation of C_{60} induced the growth of larger gains and compact thin film of perovskite with reduced defects, which led to its enhanced photovoltaic performance. Apart from that, C_{60} also participates in transportation and collection of photo-generated electrons. The optimum incorporation of C_{60} resulted in an impressive improvement in the power conversion efficiency (PCE) of champion PSC from 9.2 to 12.8%. Moreover, the C_{60}-doped PSCs exhibited improved air stability compared to undoped devices. The enhanced PCE in C_{60}-doped PSCs is a result of enhanced optical absorption and separation of photo-generated charge and their transportation in the active layer. Since the size of C_{60} molecules is of the order of nm, they easily get filled into the perovskite voids and facilitate another percolation path ways for charge carriers to transport and suppress the recombination losses via passivating the recombination centres in perovskite layers. The compact perovskite layer with larger grains led to reduced inter-granular grain boundaries with reduced defects, which restricts the fast diffusion of moisture into active layer and resulted in improved stability in device performance.

1 Introduction

Perovskite solar cells (PSCs) technology is one of the fastest growing photovoltaic technologies as they have shown very high efficiency with high cost-effectiveness [1–3]. The potential of this technology could be understood from the improvement in its power conversion efficiency (PCE) itself, which reached to a record value of ~ 25.2% just within few years [4]. Moreover, they offer low production cost, light weight and feasibility with sheet to sheet and roll-to-roll processing on flexible substrates. However, this technology is still far from the market as its overall performance is still not high enough to sought marketplace. Some of the issues that have been observe to affect their performance significantly are the grain size of perovskites crystallites, compactness of thin films, charge carriers traps, hysteresis in the I–V characteristics and poor stability [5–7]. It is important to note that usually high efficiency PSCs are prepared in a well-controlled inert environment and from perspective of commercialization they should be prepared in air. In recent years, a large volume of research activities have been carried out regarding formation of pin hole free compact perovskite layers [8–19]. It is a well reported fact that the compact and dense perovskite films without pinholes will facilitates the better pathway and reduces the charge carrier recombination between photoactive and charge transport layers [20–22]. To improve the quality of perovskite thin films and control the crystallization rate, many researchers have used additive or solvent engineering and solvent vapour treatment methods, viz. Methanol, Ammonium chloride (NH_4Cl), Lithium chloride (LiCl), 1,8-diiodooctane (DIO), Water, Methylamine (CH_3NH_2), pseudohalide Lead(II) thiocyanate ($Pb(SCN)_2$) and *N*,*N*-Dimethylmethanamide

M. S. Patel and Dhirendra K. Chaudhary are contributed equally to this work.

✉ Lokendra Kumar
lkumarau@gmail.com

[1] Molecular Electronics Research Laboratory, Physics Department, University of Allahabad, Prayagraj, U. P. 211 002, India

[2] CSIR-National Physical Laboratory, Dr. K. S. Krishnan Marg, New Delhi 110 012, India

[3] Present Address: Centre for Renewable Energy, Prof. Rajendra Singh (Rajju Bhaiya) Institute of Physical Sciences for study and Research, Veer Bahadur Singh Purvanchal University, Jaunpur 222001, India

(DMF) solvent vapour-annealing, [10–30]. Few research groups have also used fullerene derivatives to improve the PCE of PSCs. Chen et al. reported that addition of C_{60} increases the grain size and reduces the grain boundaries, benefiting the photovoltaic performance and durability of perovskite films [7]. Chao et Al. added C_{60} in toluene using antisolvent dripping process and achieved PCE of ~ 19.8% [3]. Zhang et al. reported that the devices fabricated with perovskite/pyrrole-fullerene bulk heterojunction exhibited PCE of ~ 18.9% with almost no hysteresis in current density–voltage (*J–V*) characteristics [31]. Liu et al. demonstrated that perovskite-$PC_{61}BM$ bulk heterojunction films were more uniform and denser compared to pure perovskite films [32]. Chiang et al. reported an inverted bulk heterojunction perovskite-PCBM solar cell with large grain size, high fill factor (*FF*) of 0.82 and PCE up to ~ 16.0% [12]. In our previous studies we also demonstrated that addition of PCBM led to formation of compact perovskite film with micron order grains [17]. Fang et al. reported that the addition of fullerene in perovskite solar cells increased the PCE, reduced hysteresis and improved the stability [33]. Qing et al. demonstrated an efficient strategy for the modification of TiO_2 by using fullerene that resulted in the formation of highly efficient and stable PSCs with PCE of 20.18% [34]. Sayan Bhattacharyya research group reported all-inorganic quantum dot-assisted duel modification approach which led to formation of compact perovskite layers [35]. It is important to mention here that the most of these devices were fabricated in glove boxes with well-controlled inert gas/N_2 environment.

We report here the fabrication of efficient and stable inverted PSCs with surface modulation of perovskite films. The perovskite surface was modulated by blending fullerene (C_{60}) in perovskite precursor solution in different concentrations and fabricated thin films and solar cells using them in air. From device performance comparison point of view, the solar cells were also prepared without C_{60} blending in perovskite films. The solar cells were prepared in ITO/PEDOT:PSS/$CH_3NH_3PbI_3$ or $CH_3NH_3PbI_3$:C_{60}/PCBM/Al structure under ambient atmosphere via two-step sequential spin coating method for perovskite films. Here poly-ethylene dioxythiophene: polystyrene sulfonate (PEDOT:PSS) worked as a hole transport layer (HTL) and phenyl C_{60} butyric acid methyl ester (PCBM) as an electron transport layer (ETL). Blending of C_{60} had no effect on the crystal structure of $CH_3NH_3PbI_3$ but it had a great influence on the morphology and size of the perovskite grains. It led to the formation of perovskite grains of 2–3 µm with excellent surface coverage. The optimum blending concentration of C_{60} into perovskite precursor has been observed to be 1 mg/ml, as it led to the maximum 12.80% PCE and excellent air stability.

2 Experimental details

2.1 Fabrication of perovskite films and solar cells

Indium tin oxide (ITO)-coated corning glass substrates of sheet resistivity ~ 9–10 Ω sq^{-1} were patterned using Zn metal powder and hydrochloric acid (HCl). The patterned substrates were cleaned via standard cleaning protocols; in short, the substrates were cleaned sequentially with soap solution, deionized water, acetone and isopropanol for 10 min each using ultrasonic cleaner and dried in vacuum oven. PEDOT:PSS solution was spin coated on the cleaned substrates at 3000 rpm for 30 s and heated at 140 °C for 30 min in vacuum oven. Six solutions of 0.75 M PbI_2 were prepared with blending of different concentrations of C_{60} (0, 0.25, 0.50, 1.00, 1.25 and 1.50 mg/ml) in anhydrous *N*, *N*-dimethylformamide (DMF). The PbI_2 and PbI_2:C_{60} solutions were spin coated onto PEDOT:PSS films at 3000 RPM for 60 s in air (relative humidity 43 ± 5% and temperature 20 ± 2 °C). The as-grown PbI_2 and PbI_2:C_{60} films had pale yellow colour and after annealing at 100 °C for 2 min the pale yellow colour turned into shiny yellow colour (see Fig. 1). These samples were subjected to self-cooling at room temperature for 15 min. After that, methyl ammonium iodide (CH_3NH_3I, MAI) solution was spin coated at 1000 RPM for 60 s. MAI was synthesized in our laboratory and the synthesis procedure been described in our previous reports [18, 35]. Deposition of MAI caused a rapid change in the colour of the films (during spin coating) from shiny yellow to brown. The transformation in the colour of PbI_2:C_{60} films was a bit slower. Then, 60 min annealing at 90 °C in ambient atmosphere resulted in the formation of dark brown $CH_3NH_3PbI_3$ and $CH_3NH_3PbI_3$:C_{60} films. Thereafter, 20 mg/ml solution of PCBM in chlorobenzene was spin coated on $CH_3NH_3PbI_3$ and $CH_3NH_3PbI_3$:C_{60} films at 2000 RPM for 60 s in air. As the concentration of C_{60} was very small, the thickness of the $CH_3NH_3PbI_3$ and $CH_3NH_3PbI_3$:C_{60} films were almost the same. At last, the aluminium (Al) electrode (100 nm) was deposited via thermal evaporation of Al at 0.3–0.5 Å/sec at the pressure of 5×10^{-6} torr through a shadow mask, which resulted in the active area of devices to be 0.04 cm^2. The quartz crystal thickness monitor was used to measure the thickness of deposited Al film.

2.2 Materials and device characterization

A Zeiss Field Emission Scanning Electron Microscope (FE-SEM) was used to analyse the surface morphology of the $CH_3NH_3PbI_3$ and $CH_3NH_3PbI_3$:C_{60} thin films. ImageJ image processing software was used for the determination

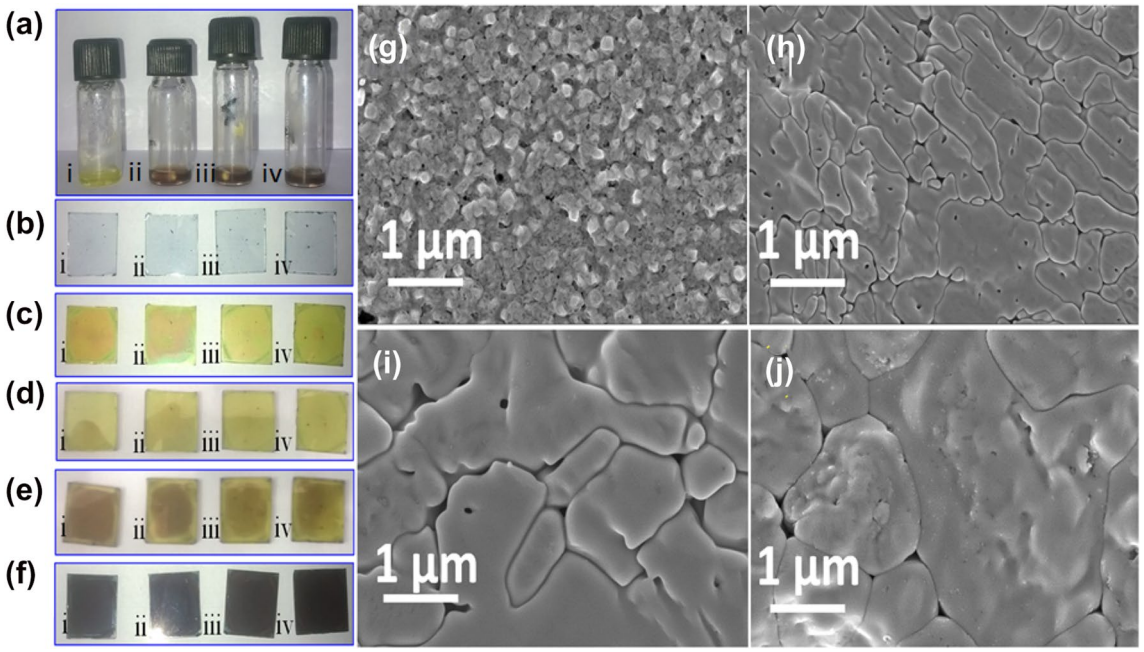

Fig. 1 **a** Photograph of PbI_2 and PbI_2:C_{60} precursor solutions with different C_{60} concentrations; (i) 0 (ii) 0.25 mg/ml (iii) 0.50 mg/ml and (iv) 1.0 mg/ml, **b** photograph of PEDOT:PSS thin films, **c** photograph of just deposited PbI_2 and PbI_2:C_{60} thin films, **d** photograph of PbI_2 and PbI_2:C_{60} thin films after heating at 100 °C for 2 min., **e** photograph of PbI_2 and PbI_2:C_{60} films after MAI deposition, **f** photograph of perovskite films with and without C_{60}. FE-SEM micrograph of **g** $CH_3NH_3PbI_3$, **h** $CH_3NH_3PbI_3$:C_{60} (0.25 mg), **i** $CH_3NH_3PbI_3$:C_{60} (0.50 mg) and **j** $CH_3NH_3PbI_3$:C_{60} (1.0 mg) thin films after heating at 90 °C for 60 min

of domain size and surface coverage area of perovskite thin films from SEM micrographs. The structural properties of $CH_3NH_3PbI_3$ and $CH_3NH_3PbI_3$:C_{60} films were studied using Proto A-XRD diffractometer equipped with CuKα (λ = 1.54 Å) radiation. Unicam 5625 UV–Vis spectrometer was used to obtain UV–Visible absorption spectra of the perovskite thin films. The steady-state photoluminescence (PL) spectra of these perovskite thin films were taken using Horiba Fluorolog with a 450 W Xenon lamp excitation source. The *J*–*V* measurements of PSCs were performed under simulated AM 1.5 sunlight from a class AAA solar simulator of Photo Emission Technology, USA (PET-SS50AAA-EM), and a Keithley-2400 source meter integrated with solar simulator. The solar simulator was calibrated for 100 mW/cm^2 light intensity using a silicon reference solar cell from the National Renewable Energy Laboratory (NREL), USA.

3 Result and discussions

Figure 1a shows the photograph of 0.75 M PbI_2 solution in DMF with doping of different C_{60} concentrations, viz. (i) 0 (ii), 0.25 mg/ml (iii) 0.50 mg/ml and (iv) 1 mg/ml. Figure 1b shows the photograph of PEDOT:PSS thin films deposited on ITO substrates. Figure 1c shows the photograph of just deposited PbI_2 and corresponding PbI_2:C_{60} thin films on PEDOT:PSS. The films turned into shiny yellow from pale yellow after thermal annealing at 90 °C (see Fig. 1d) that attributes the crystallization of PbI_2 thin film. Figure 1e shows the photograph of PbI_2 and PbI_2:C_{60} films after MAI deposition. Now these substrates were subjected to thermal annealing at 90 °C and for the growth of perovskite. The perovskite formation with pure PbI_2 film was faster than that with doped PbI_2:C_{60} films (discussed later). Figure 1f shows the photograph of perovskite films with and without C_{60}. The dark black colour of the films affirms the formation of perovskite crystals after annealing.

The FE-SEM micrograph of perovskite films are shown in Fig. 1g–j. The $CH_3NH_3PbI_3$ film exhibited several pin holes and the size of perovskite grains was very small (100–250 nm) (Fig. 1g). However, $CH_3NH_3PbI_3$:C_{60} films exhibited very large crystal grains of the order of few micrometres ranging from 1.5 to 3.5 µm. It is very clear from the SEM micrographs (see Fig. 1g–j) that as the concentration of C_{60} was increased up to 1 mg/ml, the grain size of perovskite crystals increased but for higher concentrations of C_{60} the grain size began to decrease and the grains exhibited some flakes like structure with random size distribution. Figure 2 shows the FE-SEM micrograph of perovskite film prepared by PbI_2:C_{60} precursor solution having C_{60} concentration of 1.50 mg/ml.

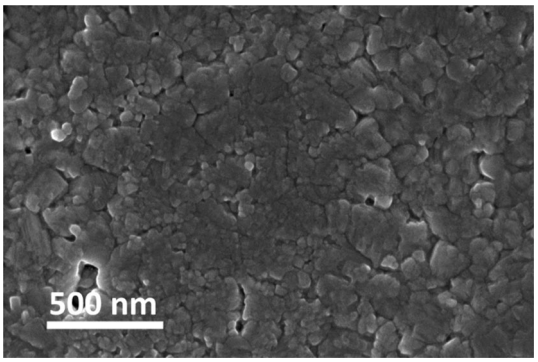

Fig. 2 FE-SEM micrograph of the $CH_3NH_3PbI_3$:C_{60} film with C_{60} concentration of 1.5 mg/ml

The reason behind difference in grain size is detailed in our previous work performed with $CH_3NH_3PbI_3$:PCBM bulk heterojunction [17]. In brief, two steps processing route for the growth of perovskite films have been used in our earlier work where perovskite is formed by intercalation of PbI_2 with MAI. The morphology of the PbI_2 film plays a significant role on the surface morphology of perovskite films. The films grown from pure PbI_2 solution are observed to be quite rough and very porous but in the presence of a C_{60} derivative the PbI_2 films grow very smooth [17]. Figure 3 shows the FE-SEM micrographs of a pure PbI_2 film and a fullerene derivate-doped PbI_2 film.

When MAI is deposited on pure PbI_2 films, due to their larger surface area and porous surface morphology, MAI diffuses into and reacts quickly with PbI_2 and it forms smaller grain size (100–250 nm). However, in case of fullerene-doped PbI_2 films, MAI diffuses into slowly-slowly and so does the film formation take place. Slow growth of perovskite crystals leads to the formation of quite smooth and dense films. Similarly, C_{60} promotes for the formation of dense PbI_2 film and fill the empty spaces in PbI_2 film. The addition C_{60} forms smooth dense bulk heterojunction $CH_3NH_3PbI_3$:C_{60} films with enhanced grain size (1.5–3.5 µm). Figure 4a shows the XRD diffractogram of $CH_3NH_3PbI_3$, $CH_3NH_3PbI_3$:C_{60} (0.25 mg), $CH_3NH_3PbI_3$:C_{60} (0.50 mg) and $CH_3NH_3PbI_3$:C_{60} (1 mg) films. The diffraction peaks at 2θ values of 14.1°, 20.0°, 24.6°, 28.4°, 31.8° and 43.2° correspond to (110), (112), (202), (220), (310) and (330) planes of tetragonal crystal structure of $CH_3NH_3PbI_3$. The peaks at 2θ value of 12.12° (denoted by * in the diffractogram) are observed due to the presence of PbI_2 in the perovskite layer.

The crystallite size was calculated from Scherrer formula and was found to be 40–53 nm. The UV–Visible absorption spectra of perovskite films with different concentrations of C_{60} are shown in Fig. 4b. For C_{60}-doped perovskite films, we observed a significant enhancement in the absorption of incident light particularly in the visible range. The increment in light absorption can be attributed to additional light absorption by C_{60} and larger perovskite grains. The photoluminescence (PL) spectra of perovskite films deposited onto PEDOT:PSS-coated ITO glass substrates are shown in Fig. 2c. The 557 nm excitation wavelength was used to excite the perovskite films. We observed the PL emission peak at ~ 782 nm for all the perovskite films. This peak is very close to the absorption band edge (~ 1.58 eV) of $CH_3NH_3PbI_3$. Along with the dominant peak at 782 nm we also observed a little peak at 748 nm (encircled in the figure) that can be attributed to the mixed phase of PbI_2 and $CH_3NH_3PbI_3$ which is also evident by XRD results. The point to be noted is that in case of $CH_3NH_3PbI_3$:C_{60} films the PL intensity got significantly passivated with a small shift (~ 10 nm) in peak position. The PL passivation in C_{60}-doped perovskite films occurred due to transfer of electrons from perovskite to C_{60} (see Fig. 3d). The PL quenching efficiency was calculated from previously report formula [36] and found that PL intensity of the perovskite films containing C_{60} is quenched by 59.52%, 68.13% and 74.65% as C_{60} concentration increases up to 1 mg/ml. The PL quenching confirms better charge separation with the Perovskite-C_{60} bulk heterojunction. The little shift in the PL peak can be attributed to the relaxation of photoexcited electrons in perovskite to its ground state through lowest unoccupied molecular orbital (LUMO) of C_{60}.

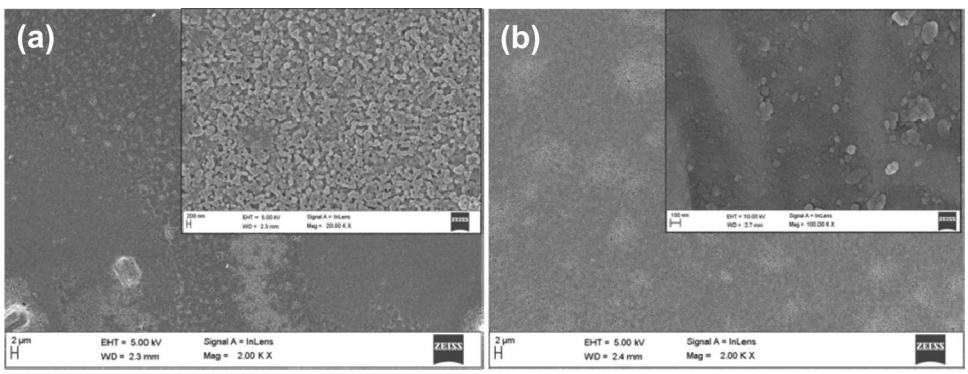

Fig. 3 FE-SEM micrographs of PbI_2 films grown from **a** pure PbI_2 solution and **b** fullerene derivative-doped PbI_2 solution in DMF [17]

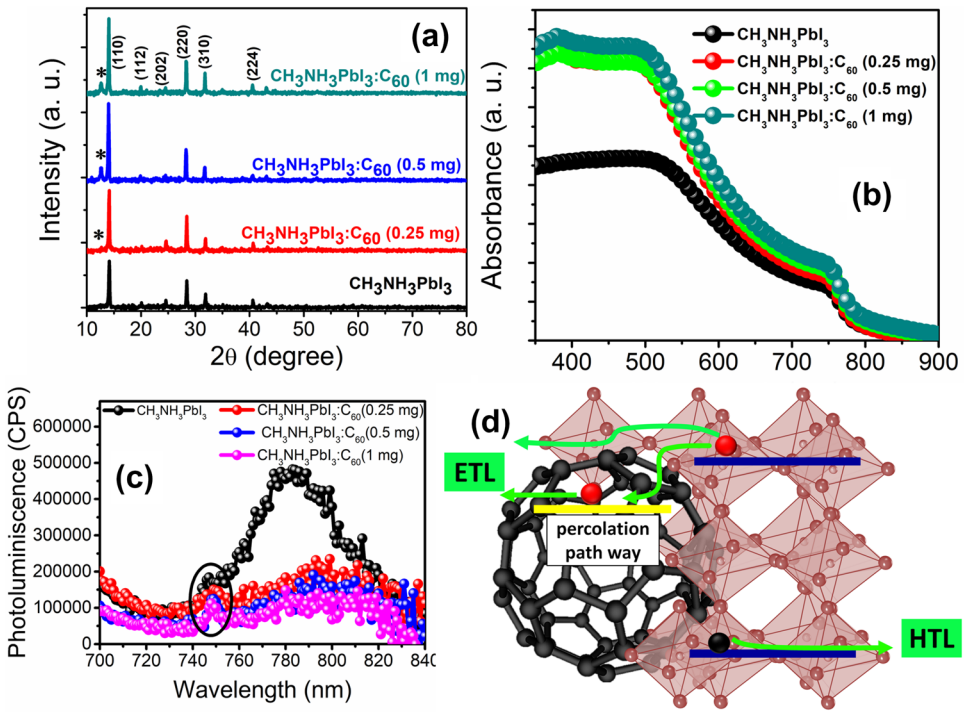

Fig. 4 **a** X-ray diffractogram, **b** UV–Visible absorbance spectra, **c** Photoluminescence spectra (excitation wavelength 557 nm) of pure $CH_3NH_3PbI_3$ and $CH_3NH_3PbI_3$:C_{60} films with different concentrations of C_{60} and **d** Schematic representation of charge transfer mechanism in $CH_3NH_3PbI_3$:C_{60} perovskite films

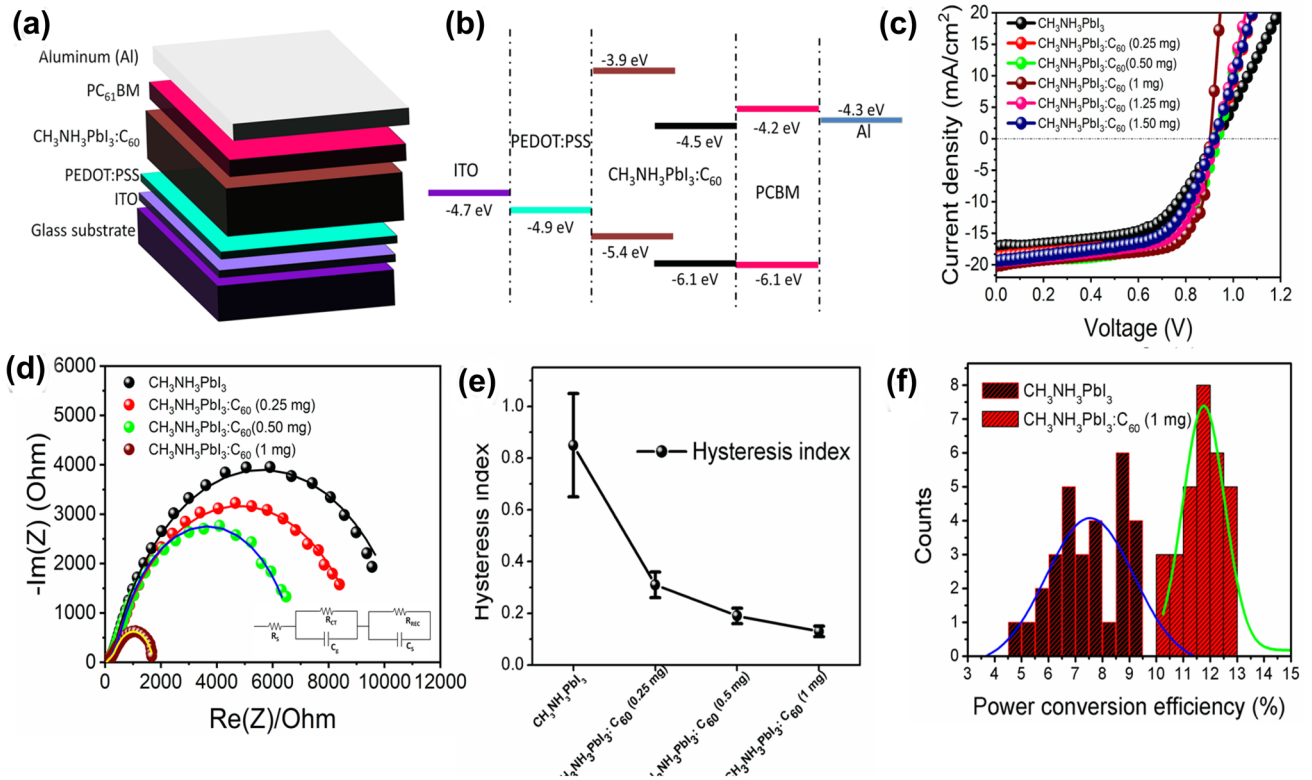

Fig. 5 Schematic representation of **a** device architecture and **b** energy level of the PSCs. **c** *J*–*V* characteristics of the devices under standard illumination conditions, **d** Nyquist plots and **e** hysteresis index plot of the PSCs with different concentrations of C_{60}. **f** Histogram plot of the efficiency of devices fabricated without and with 1 mg/ml of C_{60} concentration

Figure 5a and b shows the schematic of device architecture and energy-level diagram. The light is made incident from ITO side and then it passes through ITO/PEDOT:PSS and gets absorbed in the perovskite layer. Because of low exciton binding energy in perovskite materials, free electron–hole pairs are generated that transport via respective transport layers and get collected at respective electrodes. The photovoltaic performance of devices fabricated using $CH_3NH_3PbI_3$ and $CH_3NH_3PbI_3$:C_{60} films for different concentrations of C_{60} is shown in Fig. 5c, whereas the photovoltaic parameters of the champion devices are tabulated in Table 1. Figure 5d shows the Nyquist plots of $CH_3NH_3PbI_3$ and $CH_3NH_3PbI_3$:C_{60}-based devices. The Nyquist plots clearly show significant reduction in device series resistance upon doping of C_{60} in the perovskite films. Reduction in series resistance leads to improved charge carrier transportation and enhanced photovoltaic performance. We used the equivalent circuit shown in the inset of Fig. 3d to fit the Nyquist plots and it exhibited excellent agreement with the plots. Here R_S is external series resistance due to resistive contribution from contacts and wires, C_g is geometrical capacitance associated with the dielectric response of the perovskite, R_{CT} represents charge transfer resistance, associated with diffusion and transfer processes in perovskite layer and C_S is accumulated capacitance associated with surface charge accumulation at the interfaces and R_{rec} is the recombination resistance. On fitting, the value of R_S was found to be 66.7, 65.0, 66.2 and 64.2 Ω for $CH_3NH_3PbI_3$, $CH_3NH_3PbI_3$:C_{60} (0.25 mg), $CH_3NH_3PbI_3$:C_{60} (0.50 mg) and $CH_3NH_3PbI_3$:C_{60} (1 mg), respectively, whereas the value of R_{CT} is found to be 3717, 1959, 1569 and 1047 Ω in case of devices fabricated using $CH_3NH_3PbI_3$, $CH_3NH_3PbI_3$:C_{60} (0.25 mg), $CH_3NH_3PbI_3$:C_{60} (0.50 mg) and $CH_3NH_3PbI_3$:C_{60} (1 mg), respectively. This clearly shows the reduction of internal charge transfer resistance on increasing concentration of C_{60} in perovskite, whereas the value of R_{rec} is found to be 195, 4113, 1329 and 7198 Ω in case of $CH_3NH_3PbI_3$, $CH_3NH_3PbI_3$:C_{60} (0.25 mg), $CH_3NH_3PbI_3$:C_{60} (0.50 mg) and $CH_3NH_3PbI_3$:C_{60} (1 mg), respectively. This suggests the reduction of recombination centres in perovskite films. Figure 5e shows the plot of hysteresis index of the devices with different concentrations of C_{60}. We observed a significant reduction in the hysteresis index of the devices with increment in C_{60} concentration up to 1 mg/ml and can be attributed to the formation of compact perovskite films with larger grain size and reduced recombination centres. A histogram plot of the efficiency of $CH_3NH_3PbI_3$ and $CH_3NH_3PbI_3$:C_{60} (1 mg)-based devices is shown in Fig. 5f which shows a wide range distribution in the efficiency of $CH_3NH_3PbI_3$-based devices but in case of $CH_3NH_3PbI_3$:C_{60}-based solar cells more than ~ 90% of devices exhibited efficiency very close to best performing device which statistically suggests to believe that the devices with $CH_3NH_3PbI_3$:C_{60} are more efficient than the devices with $CH_3NH_3PbI_3$.

The values of different photovoltaic parameters (J_{SC}, V_{OC}, FF and PCE) of the champion devices with different C_{60} concentrations are shown in Fig. 6a. Figure 6b shows the variation in R_s and R_{sh} with variation in the C_{60} concentrations. We observed a significant improvement in J_{sc} and FF with increment in C_{60} concentration up to 1 mg/ml. For higher C_{60} concentration, both the J_{sc} and FF decreased slightly. The improvement in the J_{SC} and FF can be attributed to the enhancement in light absorbance and formation of larger grain size due to incorporation of C_{60}. The larger grain passivated the recombination centres within the perovskite layers. The enhanced absorbance and trap passivation contribute to the higher values of J_{SC}. Due to crystal defects, sometimes the photo-generated charge carriers get trapped within perovskite voids and the field direction of these accumulated traps is in opposite direction of the applied electric field. Therefore, this field provides hindrance in charge transport and collection and hence limits the *J*sc and FF of these devices but incorporation of C_{60} in perovskite films minimizes these effects. In case of $CH_3NH_3PbI_3$:C_{60}, due to very small molecular size of C_{60} it gets filled within perovskite voids and the C_{60} facilitates another percolation pathway for charge transportation and suppresses the charge recombination in perovskite films. V_{oc} remained almost invariant on incorporation of C_{60} for up to 1.0 mg/ml but for higher concentrations we observed very small drop in V_{oc} (~ 0.04 V drop for C_{60} concentration of 1.5 mg/ml). Above studies suggested that the optimum concentration of C_{60} to incorporate in $CH_3NH_3PbI_3$ films would be 1.0 mg/ml in 0.75 M of PbI_2 solution. We also studied the stability of solar cells incorporating C_{60} concentration of 1.0 mg/ml and their

Table 1 Photovoltaic parameters of the devices fabricated without and with different concentrations of C_{60}

Device	J_{sc} (mA/cm^2)	V_{oc} (V)	FF	Efficiency (%)	Rs (Ω cm^2)	Rsh (Ω cm^2)
$CH_3NH_3PbI_3$	17.1	0.94	0.57	9.2	14.0	319.5
$CH_3NH_3PbI_3$:C_{60}(0.25 mg)	18.6	0.94	0.61	10.1	9.0	326.5
$CH_3NH_3PbI_3$:C_{60}(0.5 mg)	19.9	0.94	0.62	11.7	7.0	398.2
$CH_3NH_3PbI_3$:C_{60}(1 mg)	20.1	0.94	0.67	12.8	4.0	442.5
$CH_3NH_3PbI_3$:C_{60}(1.25 mg)	19.8	0.92	0.64	11.28	7.6	159.0
$CH_3NH_3PbI_3$:C_{60}(1.50 mg)	19.4	0.90	0.61	10.62	7.9	145.0

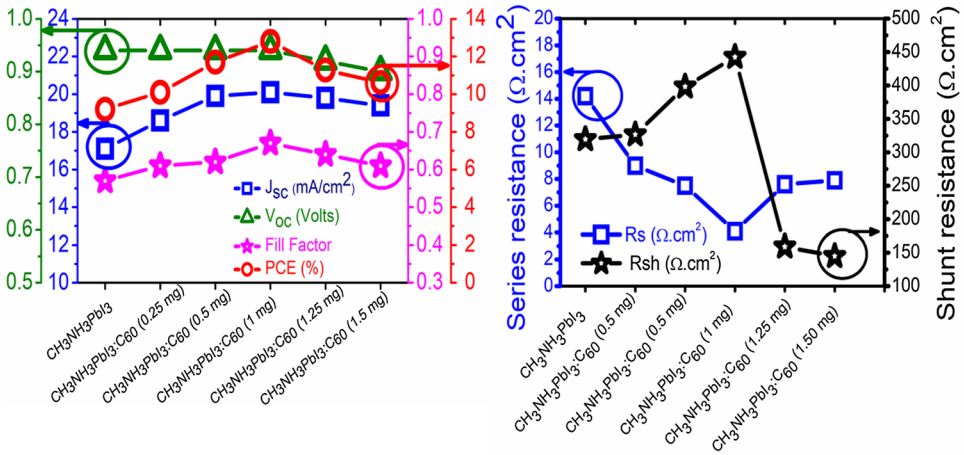

Fig. 6 **a** Photovoltaic parameters (J_{SC}, V_{OC}, FF and PCE) and **b** R_S and R_{Sh} of devices fabricated using $CH_3NH_3PbI_3$ and $CH_3NH_3PbI_3$:C_{60} with different concentrations of C_{60}

degradation profiles were compared with those without C_{60} incorporation.

The stability studies of the devices were carried out according to the International Summit on Organic Photovoltaic Stability (ISOS)-D-1 protocols. Under this protocol, the devices were stored at room temperature (22 ± 5 °C) and relative humidity 45 ± 5% in dark conditions. Devices were illuminated under standard illumination periodically for the characterization of photovoltaic performance. Figure 7 shows the degradation profiles (normalized with initial value) of PCE, FF, *J*sc and *V*oc. In case of $CH_3NH_3PbI_3$-based devices, the photovoltaic parameters decreased rapidly, whereas in case of $CH_3NH_3PbI_3$:C_{60} devices, the photovoltaic parameters decreased very slowly. In initial stage, the illumination and applied scanning potential filled the trap level which provides a better charge transport without any hindrance and contributed to partial improvement in the device performance [15]. Thereafter, devices degraded with a very slow rate of the degradation. In both cases, the ETL and HTL are identical and device processing conditions are also identical; therefore, we are assuming that the contribution of these would be same in both cases. The $CH_3NH_3PbI_3$-based devices degraded up to 60% of their initial efficiency in ~ 60 h, whereas the devices based on $CH_3NH_3PbI_3$:C_{60} took more than 260 h to degrade up to the same level. The reason behind rapid degradation in $CH_3NH_3PbI_3$ devices is the rapid diffusion of moisture into perovskite film from ambient atmosphere. Wang et al.

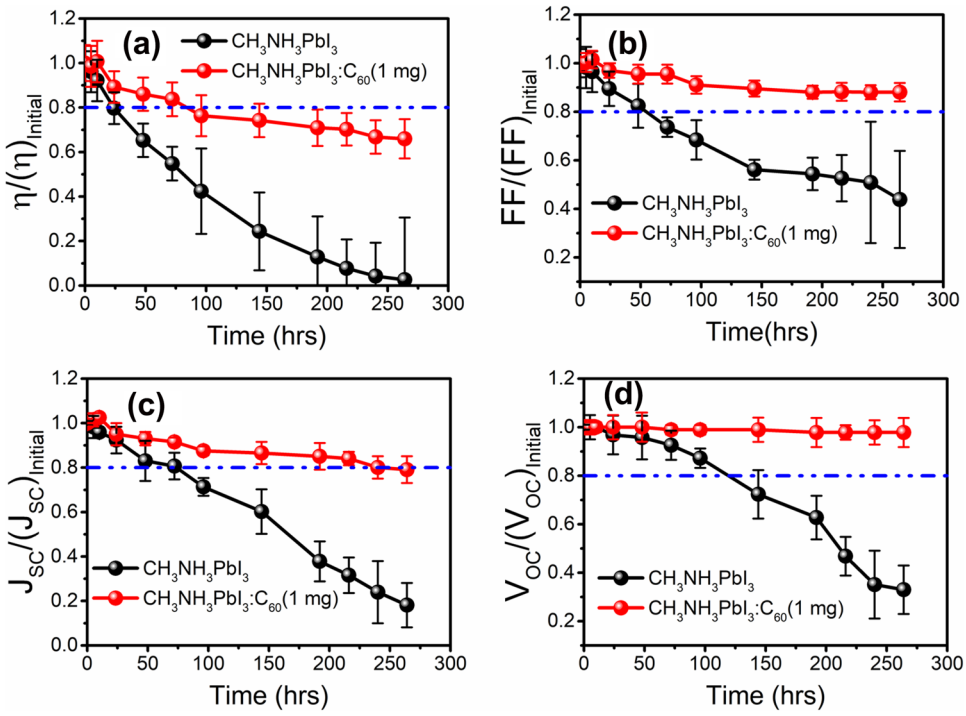

Fig. 7 Degradation profile of **a** PCE **b** FF **c** J_{sc} and **d** V_{oc} of the devices fabricated using $CH_3NH_3PbI_3$ and $CH_3NH_3PbI_3$:C_{60} (1 mg)

carried out detailed analysis on degradation of devices with small and larger grain size and proposed that perovskite grain boundaries consists an amorphous inter-granular layer which allows the faster diffusion of moisture [37]. In our case the $CH_3NH_3PbI_3$ perovskite film consisted comparatively large no. of inter-granular grain boundaries which allowed the faster moisture diffusion into perovskite films and it also contained significant no. of voids, which provide pathway for moisture diffusion into deep sites of the perovskite films in a very short time. This plays major role in rapid degradation process. However, in case of $CH_3NH_3PbI_3$:C_{60} perovskite due to the formation of larger grain size, the grain boundaries are reduced as well as the moisture-tolerant C_{60} acts as a hydrophobic interlayer and prevents further diffusion of moisture into perovskite films.

4 Conclusion

In summary, we have studied the effect of C_{60} incorporation on the growth of $CH_3NH_3PbI_3$ perovskite crystals and its impact on the photovoltaic performance as well as stability of inverted PSCs. C_{60} was incorporated in PbI_2 solutions at different concentrations that were used to grow perovskite films via two-step methods for solar cells. We found that 1.0 mg/ml blending of C_{60} in 0.75 M solution of PbI_2 leads to optimum growth of perovskite crystals with grains of few micron size. The solar cells based on $CH_3NH_3PbI_3$:C_{60} with 1.0 mg/ml blending of C_{60} exhibited PCE of 12.80%, whereas those without C_{60} exhibited a maximum PCE of 9.2%. The $CH_3NH_3PbI_3$ films without C_{60} exhibited grains of the order of ~ 100–250 nm, whereas C_{60} incorporation at the concentration of 1 mg/ml led to perovskite grains of 1.5–3.5 µm. This modification in grain size helped to achieve enhanced absorption of the incident light and better photovoltaic performance. C_{60} incorporation led to the formation of perovskite films with reduced defects and enhanced separation of photo-generated charge carriers which was evident by PL studies. Moreover, the devices with C_{60} incorporation showed better air stability when tested as per the ISOS-D-1 protocols.

Acknowledgements The financial support to this work was provided by the Department of Science & Technology under DST-FIST and UGC-CAS Phase-II grants to Physics Department, University of Allahabad.

References

1. A. Kojima, K. Teshima, Y. Shirai, T. Miyasaka, J. Am. Chem. Soc. **131**, 6050–6051 (2009)
2. N.J. Jeon, H. Na, E.H. Jung, T.-Y. Yang, Y.G. Lee, G. Kim, H.W. Shin, S. Seok, J. Lee, J. Seo, Nat. Energy **3**, 682–689 (2018)
3. C. Ji, C. Liang, H. Zhang, M. Sun, F. Sun, Q. Song, X. Zhang, D. Li, F. You, Z. He, Org. Electron. **63**, 276–282 (2018)
4. https://www.nrel.gov/pv/assets/pdfs/best-research-cell-efficiencies.20190802.pdf
5. C.H. Chiang, C.G. Wu, Nat. Photon. **10**, 196 (2016)
6. K. Deng, Z. Liu, Y. Xin, L. Li, Adv. Mater. Interfaces **5**, 1800499 (2018)
7. H.B. Chen, X.-H. Ding, X. Pan, T. Hayat, A. Alsaedi, Y. Ding, S.-Y. Dai, ACS Appl. Mater. Interfaces **10**, 2603–2611 (2018)
8. Y. Wu, X. Yang, W. Chen, Y. Yue, M. Cai, F. Xie, E. Bi, A. Islam, L. Han, Nat. Energy **1**, 16148 (2016)
9. M. Liu, M.B. Johnston, H.J. Snaith, Nature **501**, 395 (2013)
10. P. Docampo, J.M. Ball, M. Darwich, G.E. Eperon, H.J. Snaith, Nat. Commun. **4**, 2761 (2013)
11. M. Feng, S. You, N. Cheng, J. Du, Electrochim. Acta **293**, 356–363 (2019)
12. C.-H. Chiang, Z.-L. Tseng, C.G. Wu, J. Mater. Chem. A **2**, 15897–15903 (2014)
13. Y. Rahaq, M. Moussa, A. Mohammad, H. Wang, A. Hassan, J. Mater. Sci. **29**, 16426–16436 (2018)
14. D. Luo, W. Yang, Z. Wang, A. Sadhanala, Q. Hu, R. Su, R. Shivanna, G.F. Trindade, J.F. Watts, Z. Xu, T. Liu, K. Chen, F. Ye, P. Wu, L. Zhao, J. Wu, Y. Tu, Y. Zhang, X. Yang, W. Zhang, R.H. Friend, Q. Gong, H.J. Snaith, R. Zhu, Science **360**, 1442–1446 (2018)
15. J. Lei, H. Wang, F. Gao, S. Liu, Phys. Status Solidi A **215**, 1700959 (2018)
16. D. Gedamu, I.M. Asuo, D. Benetti, M. Basti, I. Ka, S.G. Cloutier, F. Rosei, R. Nechache, Sci. Rep. **8**, 12885 (2018)
17. D.K. Chaudhary, P. Kumar, L. Kumar, Chem. Phys. Lett. **685**, 210–216 (2017)
18. D.K. Chaudhary, P. Kumar, L. Kumar, RSC Adv. **6**, 94731–94738 (2016)
19. W.S. Yang, J.H. Noh, N.J. Jeon, Y.C. Kim, S. Ryu, J. Seo, S.I. Seok, Science **348**, 1234–1237 (2015)
20. H.-C. Liao, P. Guo, C.-P. Hsu, M. Lin, B. Wang, L. Zeng, W. Huang, C.M.M. Soe, W.-F. Su, M.J. Bedzyk, M.R. Wasielewski, A. Facchetti, R.P.H. Chang, M.G. Kanatzidis, T.J. Marks, Adv. Energy. Mater. **7**, 1601660 (2017)
21. H.J. Snaith, A. Abate, J.M. Ball, G.E. Eperon, T. Leijtens, N.K. Noel, S.D. Stranks, J.T.-W. Wang, K. Wojciechowski, W. Zhang, J. Phys. Chem. Lett. **5**, 1511–1515 (2014)
22. X. Li, M. Ibrahim Dar, C. Yi, J. Luo, M. Tschumi, S.M. Zakeeruddin, M.K. Nazeeruddin, H. Han, M. Grätzel, Nat. Chem. **7**, 703 (2015)
23. Y. Sheng, Y. Hu, A. Mei, P. Jiang, X. Hou, M. Duan, L. Hong, Y. Guan, Y. Rong, Y. Xiong, H. Han, J. Mater. Chem. A **4**, 16731–16736 (2016)
24. P.-W. Liang, C.-Y. Liao, C.-C. Chueh, F. Zuo, S.T. Williams, X.-K. Xin, J. Lin, A.K.-Y. Jen, Adv. Mater. **26**, 3748–3754 (2014)
25. X. Gong, M. Li, X.-B. Shi, H. Ma, Z.-K. Wang, L.-S. Liao, Adv. Funct. Mater. **25**, 6671–6678 (2015)
26. Z. Liu, J. Hu, H. Jiao, L. Li, G. Zheng, Y. Chen, Y. Huang, Q. Zhang, C. Shen, Q. Chen, H. Zhou, Adv. Mater. **29**, 1606774 (2017)
27. M.K. Kim, T. Jeon, H.I. Park, J.M. Lee, S.A. Nam, S.O. Kim, CrystEngComm **18**, 6090 (2016)
28. Z. Guo, J. Zhuang, Z. Ma, H. Xia, J. Yi, W. Zhou, H. Lu, Y. Xiang, H. Li, CrystEngComm **21**, 4753–4762 (2019)
29. C. Lan, S. Zhao, C. Zhang, W. Liu, S. Hayasea, T. Ma, CrystEngComm **18**, 9243 (2016)
30. N.-G. Park, CrystEngComm **18**, 5977 (2016)
31. Y.-N. Zhang, B. Li, L. Fu, L.-W. Yin, J. Power Sour. **419**, 27–34 (2019)
32. C. Liu, K. Wang, P. Du, C. Yi, T. Meng, X. Gong, Adv. Energy Mater. **5**, 1402024 (2015)

33. Y. Fang, C. Bi, D. Wang, J. Huang, ACS Energy Lett. **2**, 782–794 (2017)
34. Q.-Q. Ye, Z.-K. Wang, M. Li, C.-C. Zhang, K.-H. Hu, L.-S. Liao, ACS Energy Lett. **3**, 875–882 (2018)
35. D. Ghosh, D.K. Chaudhary, MdY Ali, K.K. Chauhan, S. Prodhan, S. Bhattacharya, B. Ghosh, P.K. Datta, S.C. Ray, S. Bhattacharyya, Chem. Sci. **10**, 9530–9541 (2019)
36. D.K. Chaudhary, P. Kumar, L. Kumar, J. Mater. Sci. **28**, 3451–3457 (2017)
37. Q. Wang, B. Chen, Y. Liu, Y. Deng, Y. Bai, Q. Dong, J. Huang, Energy Environ. Sci. **10**, 516–522 (2017)